Nondestructive full-field imaging XANES-PEEM analysis of cosmic grains

P. Bernhard,[1,*] J. Maul,[1] T. Berg,[1] F. Wegelin,[1] U. Ott,[2] Ch. Sudek,[2] H. Spiecker,[3] S. Merchel,[4] and G. Schönhense[1]
[1]*Institut für Physik, Staudingerweg 7, Johannes Gutenberg-Universität, D-55099 Mainz, Germany*
[2]*Max-Planck-Institut für Chemie, Becherweg 27, D-55128 Mainz, Germany*
[3]*LaVision BioTec GmbH, Meisenstrasse 65, D-33607 Bielefeld, Germany*
[4]*CEREGE, UMR CNRS 6635, F-13545 Aix en Provence, France*
(Received 29 March 2006; revised manuscript received 24 May 2006; published 1 August 2006; corrected 4 August 2006)

For chemical analysis of submicron particles, mass spectrometric methods have the disadvantage of being destructive. Thus, a nondestructive elemental and chemical mapping with a high spatial resolution prior to mass analysis is extremely valuable to precharacterize the sample. Here, first results are presented of combined XANES (x-ray absorption near-edge structure) and PEEM (photoemission electron microscopy) measurements on a cosmic grain fraction from the Murchison meteorite. This nondestructive full-field imaging method is well suited for a quantitative analysis and for a preselection prior to detailed mass spectrometric investigations with isotopic resolution/selectivity. A spectral unmixing algorithm helped to distinguish between elements in different binding surroundings and therefore to obtain lateral information about the elemental composition and the chemical structure. Individual Al_2O_3 and SiO_2 grains as well as Cr-rich grains could be identified among the majority of SiC grains. This method is suited not only for meteoritic material but can in general be applied to composite grain materials of submicron sizes.

DOI: 10.1103/PhysRevB.74.075401 PACS number(s): 79.60.−i, 97.10.Bt, 78.70.Dm, 96.50.Dj

I. INTRODUCTION

An important development in the field of cosmochemistry has been the observation that primitive meteorites contain small amounts of presolar grains, which remained unaffected by processes in the interstellar medium and during the formation of the solar system. This includes a tiny portion of the dominant silicate constituents of meteorites;[1,2] more conspicuous, however, are exotic grains of nm-sized diamonds, silicon carbide (SiC), graphite, refractory oxides (e.g., Al_2O_3, $MgAl_2O_4$), and silicon nitride (Si_3N_4). The substantial deviation in their isotope distributions from the "normal" solar abundances[3,4] (for $^{12}C/^{13}C$ in graphite and SiC, e.g., by two orders of magnitude both ways) serves as the criterion by which they are identified. Graphite and SiC grains in particular contain also a variety of diagnostic trace elements,[3] which carry not only important information about nucleosynthetic processes in stars but also about possible modes of grain formation. Most SiC grains ("mainstream grains") in all likelihood originate from carbon-rich asymptotic giant branch stars (the last major phase of life for stars less than about nine times the mass of the sun), and were expelled into the interstellar medium by stellar winds. The isotopic patterns carried by the trace elements in these grains are indicative for the nuclear "s-process" (i.e., slow-neutron capture).

So far, the main concern in the study of presolar grains has been the investigation of isotopic structures; hence, secondary ion mass spectrometry (SIMS) has been the primary method of investigation.[5,6] For trace element isotopic analyses, this has been supplemented by dedicated methods such as thermal ionization mass spectrometry[7] (TIMS), noble gas mass spectrometry,[8] and for the study of heavy trace elements in individual grains, resonance ionization mass spectrometry[9,10] (RIMS). SIMS has been used also for studying trace element patterns of SiC grains.[11] The latest development is the Nano-SIMS ion probe which is capable of mapping elemental distributions and isotopic abundances with a lateral resolution better than 100 nm.[12]

In studying grains that are both small and rare, all mass spectrometric methods have the disadvantage of being destructive. They further yield very limited information about the chemical environment of trace elements in such grains. Therefore, it would be useful to gain information on the abundance pattern of trace elements (average abundances ppm to per mill, with large grain-to-grain variations) in order to help selecting the most promising grains with respect to their elemental composition, before submitting them to destructive isotopic analysis. Synchrotron x-ray fluorescence (SXRF) has been explored towards this end with some success.[13,14] SXRF is both nondestructive and more sensitive than SIMS for elements that are not easily ionized, but it does not offer the possibility of lateral imaging and therefore of analyzing individual grains of an ensemble.

In a previous work we have explored the potential of photoelectron spectroscopy in the form of Nano-ESCA[15–17] as a tool to study the spatial distribution of elements within μm-sized SiC grains for subsequent mass spectrometric studies. Here we report on both elemental and chemical characterizations of such grains by photoemission electron microscopy, yielding the local x-ray absorption near-edge structure (XANES-PEEM).[18,19] The lateral resolution and the sensitivity thereby allowed for a clear identification of major mineral phases in individual grains.

II. SAMPLE PREPARATION AND MEASUREMENT TECHNIQUE

The investigated sample was an acid-resistant, SiC-rich residue from the Murchison meteorite. The Murchison meteorite, which fell in Australia in 1969, is a carbonaceous chondrite of the rare primitive (i.e., largely unaltered) type CM2 and thus rich (~ per mill) in matter of presolar origin.

Approximately 100 kg have been recovered, so it is also of sufficient size for a variety of detailed studies. The procedure used for the preparation was similar to those used in Ref. 20 in the preparation of the KJ SiC separate from meteorite material (named "KJ" by these authors). In brief, after dissolving the main silicate constituents of the meteorite by extensive treatment with hydrofluoric and hydrochloric acid, the surviving (mostly carbonaceous) material was treated with oxidizing agents including perchloric acid to remove more reactive carbonaceous materials. After this, the most abundant of the remaining material (nanodiamonds; approximately 1 per mill of the meteorite) was removed as a colloidal suspension. The remaining residue has been deposited on a gold foil from an aqueous suspension. The typical grain sizes range from the hundred nanometer range up to a few microns. The gold foil was provided with a grid structure, for a defined relocation of the investigated sample areas in subsequent SIMS measurements. SIMS mapping is expected to be more sensitive to trace contents, but it is both destructive and time consuming given a large field of view of the sample. Furthermore, SIMS mapping only provides little and very indirect information about chemical bonds. On the other hand, neutron scattering, e.g., could also be used for a nondestructive detection of chemical phases, even though not as an imaging tool in real space.

The sample was analyzed by XANES-PEEM in our setup described in Ref. 19. X-ray absorption near-edge structure (XANES) spectroscopy was combined with photoemission electron microscopy (PEEM). XANES probes the first empty states above the Fermi level, which are particularly sensitive to local chemical coordination and to the valence state of the absorbing atom. Thus, it is an ideal probe for elementally sensitive phase identification, provided that reference spectra exist.

A commercial microscope of the type Focus IS (Focus GmbH, Germany) was used, facilitating parallel imaging of the lateral photo- and secondary electron distribution from the sample surface with a base resolution of 20 nm. Characteristic XANES features of a particular grain are recorded as secondary electron intensity and thus show up as an enhanced intensity of that grain. For this and other contrast mechanisms in PEEM, see Ref. 21. The soft x-ray beam from the monochromator irradiates the sample surface at an angle of 65° with respect to the surface normal. The secondary electron signal is observed normal to the surface in a cone of 5° around the surface normal. Synchrotron radiation from the BESSY II beamline UE52 SGM (Ref. 22) in Berlin was taken for excitation. The energy resolution depends on the width of the exit slit (20 μm) and the used photon energy. For the energy range used here, the resolution varies between 38 meV (at $h\nu=282$ eV) and 343 meV (at $h\nu=1500$ eV). The measurements were carried out in an ultrahigh vacuum chamber with a base pressure of 8×10^{-10} mbar.

XANES-PEEM measurements provide laterally resolved spectroscopic information in the form of three-dimensional (3D) (x,y,E) image stacks, from which XANES spectra can be extracted out of any area within the investigated field of view (FoV), even after image acquisition. To correct for beamline artifacts, the extracted XANES spectra have been normalized to reference spectra, obtained from the same image stack, on the gold foil outside of the SiC grains. Gold itself exhibits no spectral features in the considered energy range but due to the sample preparation procedure, unknown admixtures in the aqueous suspension may lead to additional structures. The reference spectra from the gold foil further accounted for features from the beamline. The carbon *K* edge could not be studied because of too strong beamline artifacts caused by carbon layers on the optical elements. To obtain relative comparability of peak intensities, all XANES spectra have been normalized to the same background value at the low energy side. In the spectra shown below constant offsets have been added for a better visibility.

III. THEORY OF "LINEAR SPECTRAL UNMIXING"

In general, the 3D data stack can be defined as a multichannel image that contains for each point (x,y) and wavelength λ multiple brightnesses $I_{x,y,\lambda}$, which will be denoted as "local spectra." The idea of linear spectral unmixing is based on the assumption that the multichannel image is composed of independent sources. This means that the local spectra $I_{x,y,\lambda}$ are a linear combination of a limited number of reference spectra $S_{k,\lambda}$ where $k\in[1,k_{\max}]$. The following example illustrates the procedure: one illumination yields an image containing the emission spectra from an object composed of a varying mixture of two different substances emitting two spectra $S_{1,\lambda}$ and $S_{2,\lambda}$. In the case of no interaction between the two substances, the local spectra can be written as

$$I_{x,y,\lambda}=\rho_{x,y,1}S_{1,\lambda}+\rho_{x,y,2}S_{2\lambda}, \tag{1}$$

where $\rho_{x,y,1}$ and $\rho_{x,y,2}$ are the local densities of the substances. The task of linear spectral unmixing is to extract the linearly coefficients $\rho_{x,y,1}$ and $\rho_{x,,y,2}$ from Eq. (1) and to present them as two images revealing parts of the physical parameters describing the object. In case where the local spectra contain only two values for two spectral positions λ_1 and λ_2 the exact solution of Eq. (1) can be calculated by inverting the matrix $S_{k,\lambda}$. This is possible when $S_{1,\lambda}$ and $S_{2,\lambda}$ are linear independent. In most practical cases the number of spectral channels (i.e., number of images) is much higher than the number of reference spectra. Linear spectral unmixing then uses a least squares approximation to find the usable values for $\rho_{x,y,k}$. The equation which has to be solved for each point (x,y) is given as

$$\frac{\delta}{\delta\rho_k}|I_\lambda-\rho_kS_{k,\lambda}|^2=0. \tag{2}$$

In this sense, the linear spectral unmixing algorithm acts locally, performing a spatial analysis point by point. Sums have to be performed over indices occurring twice within a term. Equation (2) is solved by

$$\rho_k=(S_{k,\lambda}S_{j,\lambda})^{-1}S_{j,\lambda}I_\lambda. \tag{3}$$

The matrix $(S_{k,\lambda}S_{j,\lambda})$ is a square matrix of $k_{\max}\times k_{\max}$ elements and can be inverted if the spectra $S_{k,\lambda}$ are linearly independent. The advantage of spectral unmixing is that it separates the components collecting the information from all

spectral channels even if the different reference spectra look similar. Therefore, spectral unmixing allows to emphasize the spectral information included in a single point (x,y) within the spectral data stack, thus significantly enhancing the spectral signature against the background.

Linear spectral unmixing is widely used in fluorescence microscopy to eliminate the influence of overlapping emission spectra, which is seen as so-called spectral bleed in the emission channels of confocal or multiphoton microscopes.[23]

The work presented in this paper uses the commercial implementation of linear spectral unmixing within the software IMSPECTOR (LaVision BioTec GmbH, Germany). It provides the possibility to directly unmix up to four dimensional data sets $I_{x,y,z,\lambda}$ where the additional dimension z might represent, for example, an additional spatial dimension or a time dependence.

The main difficulty of spectral unmixing is the definition of the reference spectra $S_{k,\lambda}$. The easiest way to define $S_{k,\lambda}$ is to extract them out of the image itself. This is possible in cases where enough regions within the image can be identified as "pure," which means that they reveal the spectra for each component. In all other cases the reference spectra have to be generated by measurements of reference samples or by means of simulation.

IV. RESULTS

XANES-PEEM images that have been obtained by the linear spectral unmixing, which will be denoted as "unmixed XANES-PEEM images," whereas raw images taken at a single x-ray energy will be termed "X-PEEM images" in accordance with literature.

An overview image of the whole sample area taken with a scanning electron microscope is given in Fig. 1(a), which primarily shows the grid structure of the gold foil. An enlargement of the circled area is given in Fig. 1(b), showing parts of the grain sample. In comparison, Fig. 1(c) shows an UV-PEEM image of the same sample area, with a field of view (FoV) of 168 μm taken with a Hg lamp ($h\nu$=4.9 eV). The same individual particles and particle formations can be clearly recognized in both images (see, e.g., arrows in Figs. 1(b) and 1(c) for comparison). Due to the high work function of 6.5 eV for SiC (Ref. 24) the grain formations appear dark in the UV-PEEM image in Fig. 1(c). The geometry of the sample arrangement as outlined in Sec. II is sketched in Fig. 1(d).

A. XANES of the Si *K* edge

Within the same sample area as in Fig. 1(c), image stacks were taken for a broad photon energy interval in the soft x-ray range. The step width of the photon energy scan was set to 0.2 eV. Figure 2(a) shows an X-PEEM image taken on the Si *K* edge at a photon energy of 1837 eV. Several microareas (labeled *A*-*G*) are marked by circles, from which XANES spectra at different photon energies have been extracted. The size of the actual microareas ($\sim$2 μm) for spectral analysis was chosen much smaller than the circles. In Fig. 2(b), three local XANES spectra of the Si *K* edge are

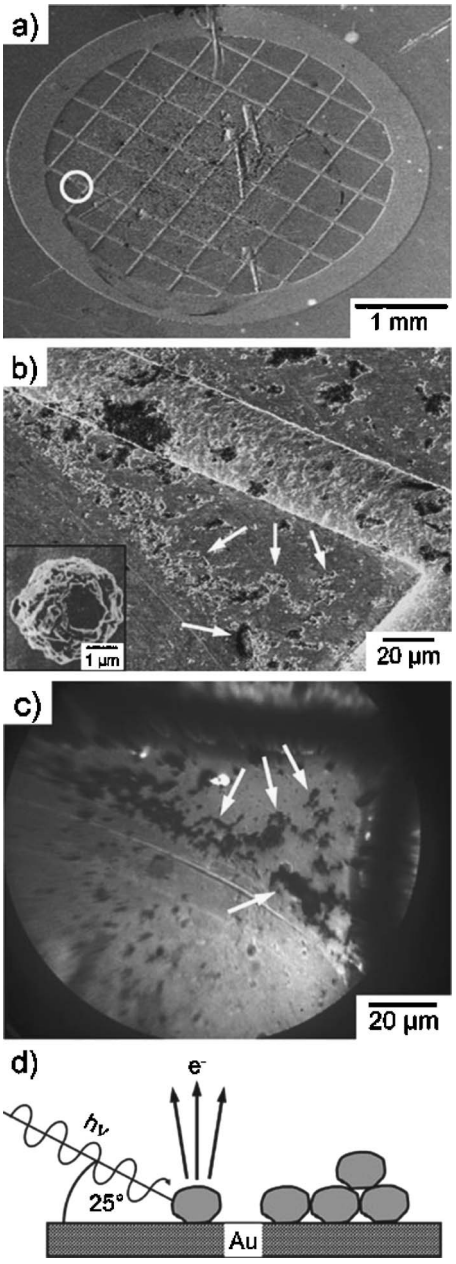

FIG. 1. (a) SEM overview image of the prepared sample. The grid structure in the gold foil serves for an easier relocation of individual grains. (b) Enlargement of the marked area; single grains and grain formations are clearly resolved within the faint contrast. The inset shows a SEM micrograph of an individual SiC grain. (c) Corresponding UV-PEEM image ($h\nu$=4.9 eV) of the same sample area. The same grains and grain formations from (b) are identified in the PEEM image. Due to the high work function, the SiC particles appear dark. (d) Experimental scheme for x-ray photoemission electron analysis.

presented, extracted from the marked areas (*A*-*C*). Two fundamentally different signatures are observed. Spectrum *A* shows a broad main peak at 1837 eV with a distinct shoulder at 1833.8 eV, a small second peak at 1843 eV, and a pronounced third peak at 1851 eV. In comparison with XANES spectra of different Si compositions,[25] spectrum *A* is found to agree perfectly with the literature spectrum of Si in SiC.

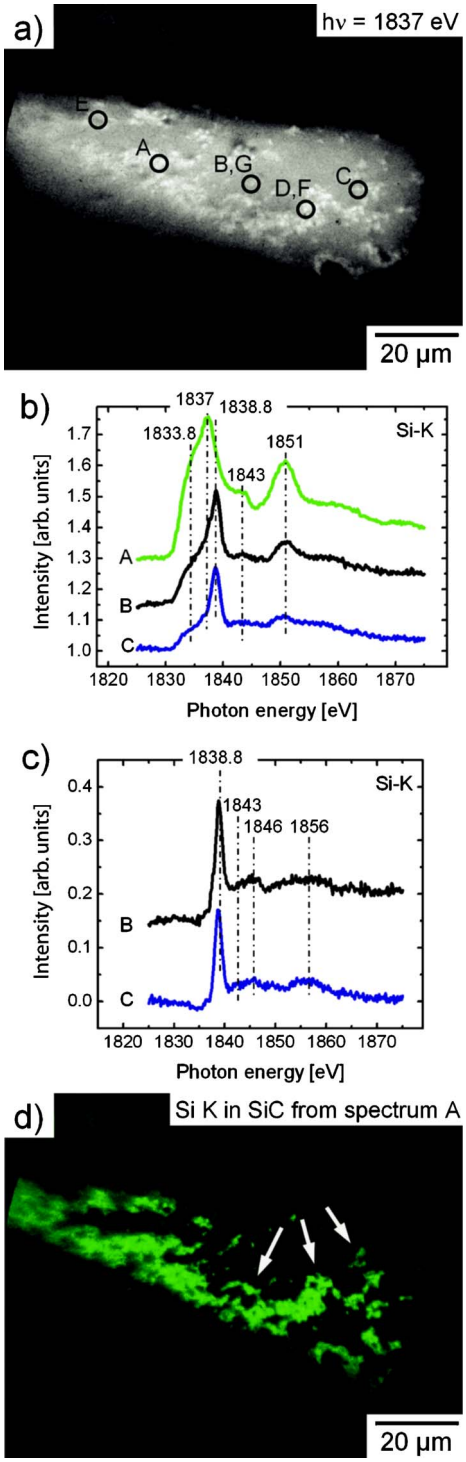

FIG. 2. (Color online) (a) PEEM image taken at the maximum of the Si *K* edge at a photon energy of 1837 eV. Marked microareas *A*-*E* identify the sample positions from which local XANES spectra have been extracted from the image stacks. XANES spectra of the Si *K* edge are given in (b). Spectrum *A* resembles Si in SiC, while spectra *B* and *C* are interpreted as a mixture of spectrum *A* and a second signature. The unmixed second signature is seen in panel (c). (d) Unmixed XANES-PEEM image of the lateral distribution of spectrum *A* as calculated by the algorithm presented in Sec. III. It shows that nearly all particles are actually composed of SiC.

Spectra *B* and *C* show a sharp peak at 1838.8 eV, with a broad shoulder towards 1832 eV and a small peak at 1851 eV. Spectra directly comparable to literature could not be found. The left shoulder of the 1838.8 eV peak and the 1851 eV peak resemble spectrum *A*. We therefore assume that microareas *B* and *C* contain grains consisting of two different chemical silicon species. Regarding spectra *B* and *C* as a mixture with a small fraction of spectrum *A*, we try to eliminate this fraction. This was done by normalizing spectrum *A* to fit the height of the peak at 1851 eV in spectra *B* and *C* before subtraction. The obtained new spectra are given in Fig. 2(c). They agree well with the literature spectra[25,26] of Si in SiO_2. Here, the shift of the SiC signature to higher energies in comparison to SiO_2 can be explained by the higher electronegativity of the (two) oxygen atoms in comparison to the (single) carbon atom in the unit cell. In particular, the fast decrease of the main peak leading to the minimum at 1841 eV clearly discriminates against Si_3N_4 that could be present in the grain fraction as well.[27]

The lateral distribution of Si bound in SiC is given in Fig. 2(d), as derived using the linear spectral unmixing algorithm. The distribution of Si in SiO_2 is given in Fig. 4(c) and will be discussed in connection with the oxygen spectra. Individual grains as well as aggregates of grains found and marked in Figs. 1(b) and 1(c) are identified again in Fig. 2(d) (see arrows). This figure also proves that the large majority of particles consist of SiC. Comparing Figs. 2(a) and 2(d), it is observed that the signal-to-noise ratio in the vicinity of the SiC is strongly increased by the spectral unmixing routine.

This spectral unmixing algorithm applied remarkably well to a majority of grain sizes, as it is apparent from, e.g., Fig. 2(a). Thus, changes in the absorption spectra due to the three-dimensional extension of the grains appear to be negligible, even in the presence of the high PEEM extraction voltages.

B. XANES of the Al and O *K* edges

The spectral information of the marked microareas (*D*,*E*) in Fig. 2(a) within the energy interval of the Al *K* edge is given in Fig. 3(a). A dominant sharp peak at 1560 eV can be recognized, as well as a broader and smaller peak at 1564.2 eV and a small feature at 1568.8 eV. Within the given energy range, only this Al signature could be found. In Mo and Ching,[28] calculated and measured energy-loss near-edge structures (ELNES) are presented for the aluminum-containing oxides α-Al_2O_3 (corundum) and $MgAl_2O_4$ (Mg-Al-spinel). ELNES analysis usually reproduces the same structure as XANES. Both investigated aluminum compounds are known to be present as robust, i.e., acid-resistant mineral contributions within the Murchison meteorite sample.[3] The comparison of the Al *K* spectra corroborates the identification of corundum, and the clear exclusion of Mg-Al-spinel for the inspected grain.[28] The unmixed XANES-PEEM image showing the lateral distribution of spectrum *D* is given in Fig. 4(a).

Figure 3(b) gives XANES spectra *F* and *G* of the O *K* edge, extracted from the corresponding microareas defined in Fig. 2(a). Again, spectra with two different signatures are

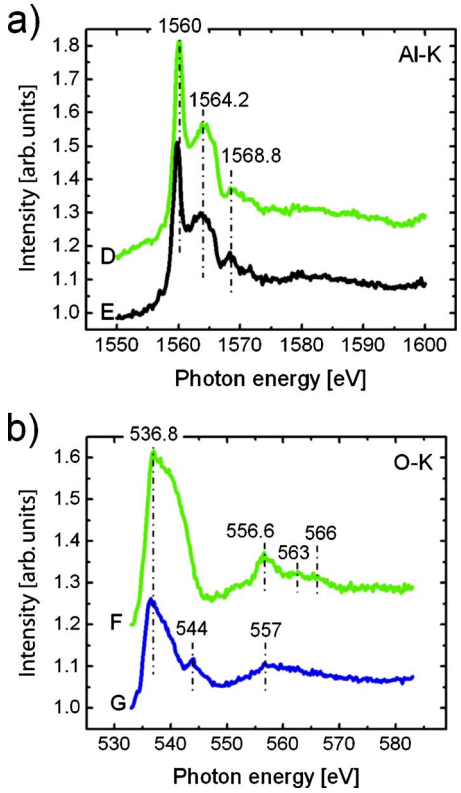

FIG. 3. (Color online) (a) XANES spectra of the Al *K* edge, extracted from the microareas *D* and *E* in Fig. 2(a). Both spectra resemble Al bound in Al_2O_3. (b) XANES spectra of the oxygen *K* edge. Spectrum F, extracted from area F in Fig. 2(a) seems to be similar to oxygen in Al_2O_3, spectrum *G* represents oxygen bound in SiO_2.

observed. For spectrum *F* with its broad peak at 536.8 eV, a second peak at 556.6 eV, and two weaker signals at about 563 and 566 eV, we conclude that it represents oxygen in α-Al_2O_3 as our spectrum fits rather well to calculated spectra.[28] Additionally and independently, this interpretation is supported by the agreement with the Al signature (see above). Spectrum *G*, with its main peak at 536.8 eV as well as the distinct peak at 544 eV and the broader feature around 557 eV, is in accordance with literature spectra of oxygen in SiO_2 as presented by Gilbert *et al.*[26] and Wu *et al.*[29]

The lateral distribution of spectra *F* and *G* is given in Figs. 4(b) and 4(d) respectively. The differences between the spectra *F* and *G*, which are not striking at first glance, are well resolved by the linear spectral unmixing, leading to a clear distinction of the corresponding grains in the unmixed XANES-PEEM images in Figs. 4(b) and 4(d) with excellent signal-to-noise ratio and zero crosstalk.

In comparing the four unmixed images in Fig. 4, it is easily recognized that the major signals in Figs. 4(a) and 4(b) are well correlated. For better visibility, several matching spots have been marked. It can be concluded that spectrum *F* in Fig. 3(b) indeed represents oxygen in Al_2O_3, and that Figs. 4(a) and 4(b) show the lateral distribution of Al_2O_3 seen from the distribution of aluminium and oxygen, respectively. Grains visible in Fig. 4(c) all show up in Fig. 4(d). We conclude that the grains visible in Fig. 4(c) show the lateral

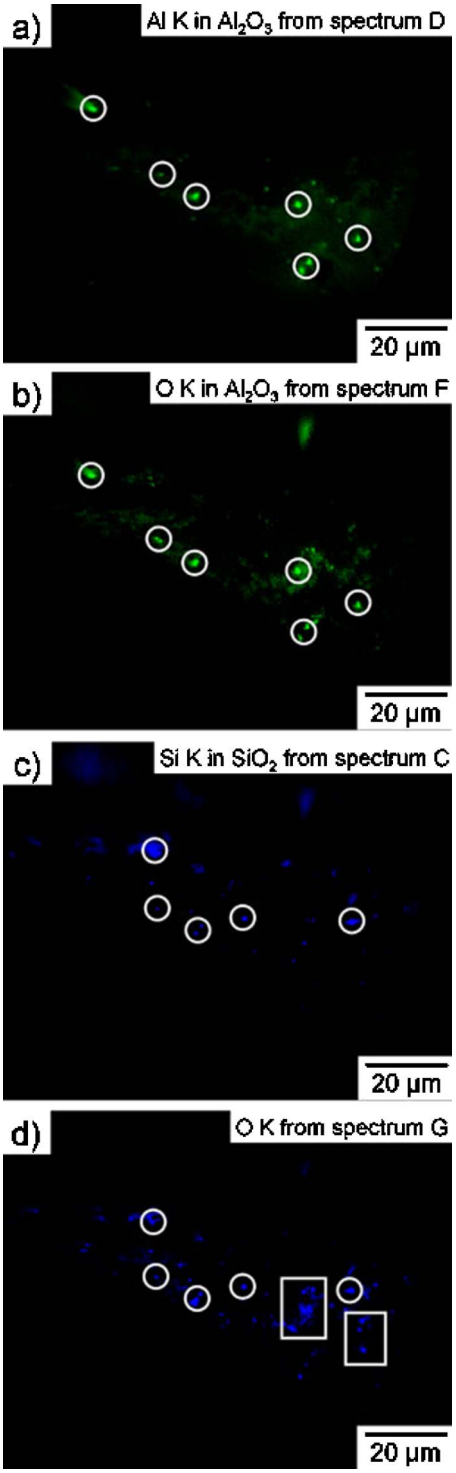

FIG. 4. (Color online) (a) and (b) Unmixed XANES-PEEM images showing the correlated lateral distribution of spectra *D* and *F*, respectively. The main signals have been marked by circles. (a) and (b) show the lateral distribution of Al_2O_3 grains. Similarly, also the main signals in the unmixed images (c) and (d) match rather well. They show the lateral distribution of SiO_2, from the correlated spatial Si *K* (c) and O *K* (d) signature.

distribution of SiO_2, because silicon correlates with the corresponding distribution of oxygen. Figure 4(d) further shows bright grains that are absent in Fig. 4(c), as seen from group

of grains marked by squares. Evidently, at least one additional oxide species is present in these areas.

C. XANES of the Cr L_2/L_3 and the O K edge

Using a slightly different FoV, measurements have been performed over an energy range from 525 eV up to 592 eV, to completely cover the O K and the Cr L_2/L_3 edges. The step width was increased from 0.2 eV to 0.5 eV. In Fig. 5(a) an X-PEEM image is given, taken at the Cr L_3 edge at 576 eV. Four spectra (H, K, L, M), extracted from different microareas as labeled in Fig. 5(a) have been plotted in Fig. 5(b). Spectra H and M have been enlarged by a factor of three for a better comparability of the four spectra. They show markedly different XANES signatures of the O K edge. In spectrum H we see next to the main peak at 537 eV a narrow feature at 540.5 eV and a broad structure between 555 and 565 eV followed by the pronounced L_2/L_3 edges of Cr. The significant structure in the O K edge indicates that the chromium is oxidized. This is proven by the L_3 and the L_2 edges, as both have a double peak structure. The peak positions are about 574.5 eV, 576 eV, 584 eV, and 586 eV. The second peak within the L_3 edge is larger than the first one and vice versa for the L_2 edge, agreeing well with literature data for oxidized chromium (Ref. 30). The lateral distribution of the Cr XANES signature is given in Fig. 5(c). Most likely here the Cr appears in the compound $FeCr_2O_4$ (chromite). This compound is known to be present in meteoritic material and to have significant resistance to acid treatment.[31] It is expected to survive the first steps of the chemical extraction, but not the full separation procedure. It is possible, nevertheless, that some few grains survived the procedure.

Spectrum K resembles spectrum F in Fig. 3(b), which already has been identified as oxygen in Al_2O_3. The lateral distribution of spectrum K is similar to that of Fig. 4(b), given the different FoV.

Spectrum L reveals a signature that has not been investigated before. The reason for this is that its general line shape is similar but not equal to the one of spectrum M. The main difference is the sharp peak at 529.5 eV. Since we expected no signals below 533 V, the earlier measurement was done from 533 eV to 583 eV so that this peak was missed. Another difference is an indication for a splitting of the main peak by 1.5 eV, which is small but recognizable and could not be seen in spectrum G and in spectrum M. XANES spectra of the O K edge of FeO as presented by Wu *et al.*[32] bear a significant single sharp peak at around 6.9 eV below the main peak at 538.7 eV. The main peak itself shows a splitting by 1.8 eV and two further features appear at 7 eV (a shoulder) and 21 eV (a broad peak) above the main peak. Although there is an offset in the absolute energy values in the spectra from Wu *et al.* compared to ours, the relative energetic distances between single features fit well, except for the shoulder at 7 eV above the main peak, which does not appear in spectrum L. Based on these agreements we suggest that spectrum M shows the O K edge of FeO. We have observed that an uncompleted dissolving procedure of $FeCr_2O_4$ primarily ends with oxidized chromium in the re-

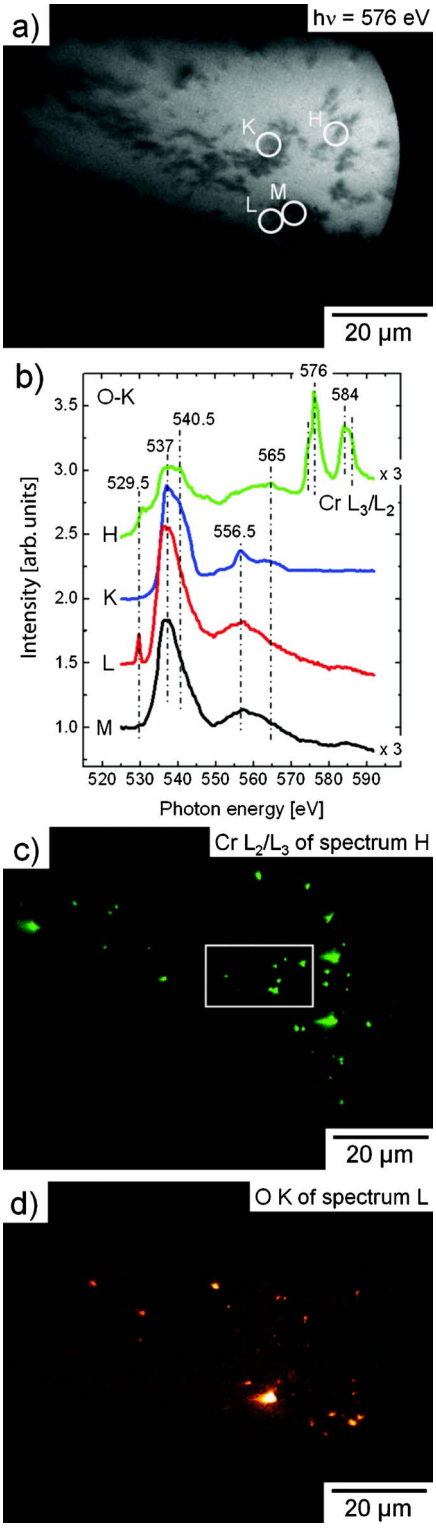

FIG. 5. (Color online) (a) X-PEEM image taken at the maximum of the Cr L_3 edge at a photon energy of 576 eV in a slightly different FoV. Marked microareas identify the sample positions, from which local XANES spectra have been extracted from the image stacks. (b) Corresponding spectra in the region of the oxygen K and Cr $L_{2/3}$ edges. (c) and (d) unmixed XANES-PEEM images of the Cr $L_{2/3}$ features in spectrum H and the oxygen species in spectrum L, respectively. The marked area in (c) is used for further analysis.

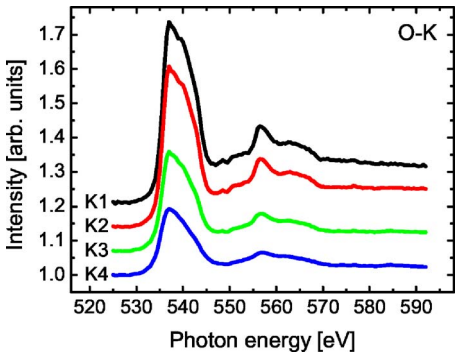

FIG. 6. (Color online) Local XANES spectra extracted from different field of views around the sample position *K* in Fig. 5(b) with a frame size of 0.28 μm (FoV of *K*1), 0.56 μm (FoV of *K*2), 1.06 μm (FoV of *K*3), and 2.12 μm (FoV of *K*4).

siduum and all of the Fe in the discarded solution. Therefore it is believed that the detected FeO or Fe_2O_3 grains do not originate from material of the Murchison meteorite, but rather have to be seen as a contamination by terrestrial material after sample preparation. The signature of spectrum *L* appears only in a very small number of grains within the investigated FoV, as visible by the lateral distribution of this XANES signature, given in Fig. 5(d).

Spectrum *M* is considered to be the same as spectrum *G* in Fig. 3(b) representing oxygen in SiO_2. The differences between these two spectra, mainly the absence of the minor peak at 544 eV, are believed to appear due to the larger step width of 0.5 eV instead of 0.2 eV. The lateral distribution of spectrum *M* corresponds to the one of spectrum *G* in Fig. 4(d).

Finally, for a demonstration of the methodological reliability, XANES O *K* spectra were extracted from areas of interest of different sizes. The microscope FoV has not been changed. In Fig. 6, the areas used to extract the spectral signature around position *K* in Fig. 5(b) ranged between 0.28 μm and 2.12 μm in one dimension, covering about two orders of magnitude in a lateral dimension, correspondingly. Here, the lateral dimension is understood as the number of pixels used for the different evaluations of the XANES spectra by implementation of the spectral unmixing algorithm. As evident from Fig. 6, all spectral scans exhibit the same signatures qualitatively. As to be expected, they basically differ in their signal-to-noise ratios.

D. Determination of smallest grain sizes

The size of three-dimensional objects can be extracted from line scans from PEEM images.[33] This method is used to estimate the size of some of the smallest grains detected. For this, Fig. 5(c) was analyzed because the electron emitting grains appear separated from each other and bear some of the smallest signal spots among them. Figure 7(a) shows an enlargement of the marked area of Fig. 5(c). Different bright spots have been labeled (1–4). Line scans through the center of each spot are presented in Fig. 7(b). The intensity distributions of the two smallest particles (3, 4) consist of no more than eight image pixels. For the grain sizes the full width at half maximum (FWHM) of the intensity distributions are

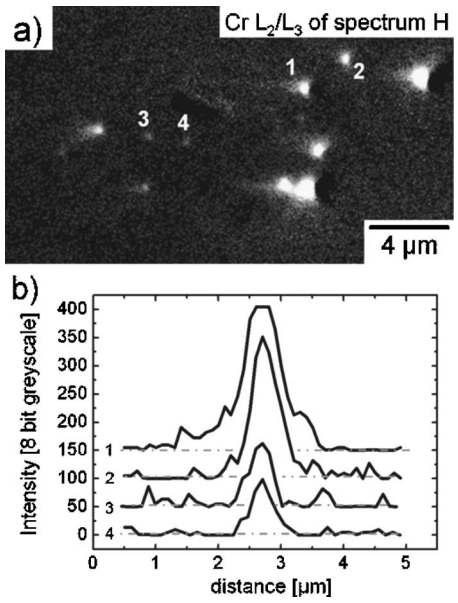

FIG. 7. (a) Enlargement of the marked area in Fig. 5(c). (b) Line scan through the center of the labeled spots in (a). The dashed lines through the average values of the noise levels represent the baselines. The distance of the two crossing points with the intensity distribution measures to the grain size.

taken, which ends up with values for the grains 1–4 of 690 nm, 500 nm, 460 nm, and 370 nm, respectively. Due to some neglected effects (e.g., apparent size changing due to work-function differences[34]) these values should be seen as approximations. The clear contrasts in the spectrally unmixed image of Fig. 7(a) much enhances both the detection and the localization of single grains. This identification is additionally supported by the shadowing of the grains due to the grazing incidence of the synchrotron radiation. This issue is clearly visible in Fig. 7(a) and was previously reported by Heun *et al.*[35] In the present study, only a medium magnification mode of the microscope was taken in order to access a large field of view. Use of the highest magnification should enhance the instrumental capability to detect the smallest grain sizes.

V. CONCLUSION

A fraction of cosmic grains extracted from the Murchison meteorite has been investigated by a full-field imaging method with high chemical specificity. XANES-PEEM in combination with the linear spectral unmixing algorithm is a powerful tool to distinguish elements in different binding surroundings and to image their lateral distribution maps separately from each other. In particular for XANES signatures with only small differences, such as the O *K* edge of Al_2O_3 and SiO_2, this method bears clear advantages. Signals of the order of the noise can be detected, provided that they still comprise a significant XANES structure. $FeCr_2O_4$ grains with sizes of around 370 nm could be detected. Therefore, XANES-PEEM in combination with the linear spectral unmixing algorithm offers an unprecedented nondestructive access to the chemical characterization of cosmic grains. The method can also be applied to the characterization of mineral

phases recently discovered in meteorites, such as supernova olivine[36] and possibly superhard carbon.[37] The method can also be applied to other materials such as grains collected by the stardust mission, and in general to all kinds of composite grain material which require submicron lateral resolution together with the chemical information.

ACKNOWLEDGMENTS

Thanks are due to the staff of BESSY for excellent beamline support. The project was funded by the "Materialwissenschaftliche Forschungszentrum (MWFZ) Mainz," and to P. Hoppe for a SEM micrograph of an individual SiC grain.

*Corresponding author. Email address: bernharp@uni-mail.de

[1] A. N. Nguyen and E. Zinner, Science **303**, 1496 (2004).
[2] S. Mostefaoui and P. Hoppe, Astrophys. J. **613**, L149 (2004).
[3] U. Ott, Nature (London) **364**, 25 (1993).
[4] E. Zinner, Annu. Rev. Earth Planet Sci. **26**, 147 (1998).
[5] E. Zinner, Meteorit. Planet. Sci. **33**, 549 (1998).
[6] P. Hoppe and E. Zinner, J. Geophys. Res., [Planets] **105**, 10371 (2000).
[7] U. Ott and F. Begemann, Astrophys. J. **353**, L57 (1990).
[8] R. S. Lewis, S. Amari, and E. Anders, Geochim. Cosmochim. Acta **58**, 471 (1994).
[9] G. K. Nicolussi, A. M. Davis, M. J. Pellin, R. S. Lewis, R. N. Clayton, and S. Amari, Science **277**, 1281 (1997).
[10] M. R. Savina, A. M. Davis, C. E. Tripa, M. J. Pellin, R. N. Clayton, R. S. Lewis, S. Amari, R. Gallino, and M. Lugaro, Geochim. Cosmochim. Acta **67**, 3291 (2003).
[11] S. Amari, P. Hoppe, E. Zinner, and R. S. Lewis, Meteoritics **30**, 679 (1995).
[12] P. Hoppe, U. Ott, and G. W. Lugmair, New Astron. Rev. **48**, 171 (2004).
[13] Y. Kashiv, Z. Cai, B. Lai, S. R. Sutton, R. S. Lewis, A. M. Davis, R. N. Clayton, and M. J. Pellin, Lunar Planet. Sci. **32**, Abstract #2192 (2001).
[14] Y. Kashiv, Z. Cai, B. Lai, S. R. Sutton, R. S. Lewis, A. M. Davis, R. N. Clayton, and M. J. Pellin, Lunar Planet. Sci. **33**, Abstract #2056 (2002).
[15] U. Ott, Ch. Sudek, J. Maul, P. Bernhard, and G. Schönhense, Lunar Planet. Sci. **36**, Abstract #1294 (2005).
[16] P. Bernhard, J. Maul, U. Ott, Ch. Sudek, M. Escher, N. Weber, M. Merkel, B. Krömker, D. Funnemann, and G. Schönhense, Nucl. Instrum. Methods Phys. Res. B **246**, 275 (2005).
[17] M. Escher, N. Weber, M. Merkel, Ch. Ziehten, P. Bernhard, G. Schönhense, S. Schmidt, F. Forster, F. Reinert, B. Krömker, and D. Funnemann, J. Phys.: Condens. Matter **17**, 1329 (2005);. M. Escher, N. Weber, M. Merkel, B. Krömker, D. Funnemann, S. Schmidt, F. Reinert, F. Forster, S. Hüfner, P. Bernhard, Ch. Ziethen, H. J. Elmers, and G. Schönhense, J. Electron Spectrosc. Relat. Phenom. **144-147**, 1179 (2005).
[18] B. P. Tonner and G. R. Harp, Rev. Sci. Instrum. **59**, 853 (1988).
[19] Ch. Ziethen, O. Schmidt, G. K. L. Marx, G. Schönhense, R. Frömter, J. Gilles, J. Kirschner, C. M. Schneider, and O. Gröning, J. Electron Spectrosc. Relat. Phenom. **107**, 261 (2000).
[20] S. Amari, R. S. Lewis, and E. Anders, Geochim. Cosmochim. Acta **58**, 459 (1994).
[21] C. M. Schneider and G. Schönhense, Rep. Prog. Phys. **65**, 1785 (2002).
[22] F. Senf, F. Eggenstein, U. Flechsig, R. Follath, S. Hartlaub, H. Lammert, T. Noll, J. S. Schmidt, G. Reichardt, O. Schwarzkopf, M. Weiss, T. Zeschke, and W. Gudat, Nucl. Instrum. Methods Phys. Res. A **467-468**, 474 (2001).
[23] R. Neher and E. Neher, J. Microsc. **213**, 46 (2004).
[24] G. Brauer, W. Anwand, E.-M. Nicht, J. Kuriplach, M. Sob, N. Wagner, P. G. Coleman, M. J. Puska, and T. Korhonen, Phys. Rev. B **54**, 2512 (1996).
[25] J. Wong, G. N. George, J. Pickering, Z. U. Rek, M. Rowen, T. Tanaka, G. H. Via, B. DeVries, D. W. E. Vaughan, and G. E. Brown Jr., Solid State Commun. **92**, 559 (1994).
[26] B. Gilbert, B. H. Frazer, F. Naab, J. Fournelle, J. W. Valley, and G. De Stasio, Am. Mineral. **88**, 763 (2003).
[27] S. Mastefaoui and P. Hoppe, Astrophys. J. **613**, L149 (2004).
[28] S.-D. Mo and W. Y. Ching, Phys. Rev. B **62**, 7901 (2000).
[29] Z. Y. Wu, F. Jollet, and F. Seifert, J. Phys.: Condens. Matter **10**, 8083 (1998).
[30] H. J. Elmers, G. H. Fecher, D. Valdaitsev, S. A. Nepijko, A. Gloskovskii, G. Jakob, G. Schönhense, S. Wurmehl, T. Block, C. Felser, P.-C. Hsu, W.-L. Tsai, and S. Cramm, Phys. Rev. B **67**, 104412 (2003).
[31] U. Ott, R. Mack, and S. Chang, Geochim. Cosmochim. Acta **45**, 1751 (1981).
[32] Z. Y. Wu, S. Gota, F. Jollet, M. Pollak, M. Gautier-Soyer, and C. R. Natoli, Phys. Rev. B **55**, 2570 (1997).
[33] S. A. Nepijko, N. N. Sedov, O. Schmidt, G. Schönhense, X. Bao, and W. Huang, J. Microsc. **202**, 480 (2001).
[34] S. A. Nepijko, N. N. Sedov, O. Schmidt, G. H. Fecher, and G. Schönhense, Ann. Phys. (Paris) **11**, 39 (2002).
[35] S. Heun, Y. Watanabe, B. Ressel, D. Bottomley, Th. Schmidt, and K. C. Prince, Phys. Rev. B **63**, 125335 (2001).
[36] S. Messenger, L. P. Keller, and D. S. Lauretta, Science **309**, 737 (2005).
[37] N. Dubronnskaia, L. Dubronnsky, W. Crichton, F. Langenhorst, and A. Richter, Appl. Phys. Lett. **87**, 083106 (2005).